Versatile Modeling Of Deformation (VMOD) Inversion Framework: Application to 20 Years of Observations at Westdahl Volcano and Fisher Caldera, Alaska, US

M. Angarita[1] , R. Grapenthin[1] , S. Henderson[2] , M. Christoffersen[1], and K. R. Anderson[3]

[1]Geophysical Institute and Department of Geosciences, University of Alaska Fairbanks, Fairbanks, AK, USA, [2]Department of Earth and Space Sciences, University of Washington, Seattle, WA, USA, [3]U.S. Geological Survey, Volcano Science Center, Moffett Field, CA, USA

Abstract We developed an open source, extensible Python-based framework, that we call the Versatile Modeling Of Deformation (VMOD), for forward and inverse modeling of crustal deformation sources. VMOD abstracts from specific source model implementations, data types and inversion methods. We implement the most common geodetic source models which can be combined to model and analyze multi-source deformation. VMOD supports Global Navigation Satellite System (GNSS), InSAR, electronic distance measurement, Leveling and tilt data. To infer source characteristics from observations, VMOD implements non-linear least squares and Markov Chain Monte-Carlo Bayesian inversions, including joint inversions using different sources of data. VMOD's structure allows for easy integration of new geodetic models, data types, and inversion strategies. We benchmark the forward models against other published results and the inversion approaches against other implementations. We apply VMOD to analyze deformation at Unimak Island, Alaska, observed with continuous and campaign GNSS, and ascending and descending InSAR time series generated from Sentinel-1 satellite radar acquisitions. These data show an inflation pattern at Westdahl volcano and subsidence at Fisher Caldera. We use VMOD to test a range of source models by jointly inverting the GNSS and InSAR data sets. Our final model simultaneously constrains the parameters of two sources. Our results reveal a depressurizing spheroid under Fisher Caldera ~4–6 km deep, contracting at a rate of ~2–3 Mm^3/yr, and a pressurizing spherical source underneath Westdahl volcano ~6–8 km deep, inflating at ~5 Mm^3/yr. This and past applications of VMOD to volcanic unrest benefit from an extensible framework which supports jointly inversions of data sets for parameters of easily composable multi-source models.

Plain Language Summary We developed a computational framework called the Versatile Modeling Of Deformation (VMOD) to calculate surface deformation created by buried pressure, tensile and shear sources, or find parameter values for a model that fits observed surface deformation. The framework has three main components. One component handles the model, one component handles the data, and the remaining component handles the algorithm that finds the most probable values for the parameters of a given model. Deformation can be observed using different techniques such as Global Navigation Satellite System (GNSS) or satellite images. The framework supports most of these techniques and allows users to add new techniques or deformation models. We validate our framework with literature results and contrast it with similar software used in the volcano deformation community. We apply the framework to analyze a deformation episode at Westdahl volcano and Fisher Caldera on Unimak Island, Alaska. The deformation is captured by GNSS and satellite radar images. Our results suggest a deflating spheroid ~4–6 km deep with a rate of ~2–3 Mm^3/yr for Fisher Caldera and a inflating spherical source underneath Westdahl volcano ~6–8 km deep, at a rate of ~5 Mm^3/yr. This and previous experiences highlight the advantages of multi-source model deformation observations from different techniques.

1. Introduction

Crustal deformation can have multiple sources including tectonic forces, anthropogenic processes, and volcanic or magma dynamics. Observations of co-seismic deformation can help resolve the slip distribution on faults during earthquakes (e.g., J. L. Elliott et al., 2022) while interseismic deformation helps to quantify long-term fault slip rates (e.g., J. Elliott & Freymueller, 2020) or the spatial extent and degree of fault coupling (e.g., Xiao et al., 2021). For oil/gas extraction and fluid injection, deformation observations can constrain reservoir dynamics

and media properties (Q. Yang et al., 2015). Geodetic monitoring in the vicinity of volcanoes (e.g., Fernández et al., 2017) considers that deformation of the surface is due to magma dynamics at depth (e.g., Biggs & Pritchard, 2017; Sigmundsson et al., 2015), processes in the hydrothermal system (e.g., Fournier & Chardot, 2012; Yunjun et al., 2021), or deposition and post-deposition processes (Angarita et al., 2022; Ebmeier et al., 2012). As a consequence, geodesists expect to gain insights into subsurface processes (Poland et al., 2006). Currently, the most widely used techniques to observe surface deformation include the Global Navigation Satellite System (GNSS, which includes GPS), Synthetic Aperture Radar (SAR) and Interferometry of SAR acquisition pairs (InSAR), and in some places tiltmeters.

There has been an effort to analyze observations from geodetic monitoring networks with increasingly sophisticated models in order to improve our understanding of the dynamic behavior of subsurface processes (e.g., Cashman & Sparks, 2013). However, modeling of surface deformation usually begins with simplifying assumptions which allow the application of approximate analytical kinematic solutions to estimate source parameters such as dimensions, locations, and pressure changes. The drawbacks of simplified models are well known (e.g., Masterlark, 2003, 2007). For instance, the analytical models do not account for heterogeneity in the crust (Albright & Gregg, 2020; Heap et al., 2020) or topography (Crozier et al., 2023). However, the continued use of these models, especially in monitoring settings, is driven by the scarcity of (time-varying) observations, poor a-priori information on the host rock properties, model uniqueness issues, and the increased computational resources required by more complex models.

Each of the techniques used to observe crustal deformation offers advantages and disadvantages. GNSS can resolve three-dimensional displacements with millimeter-level precision. In many places long term time series (several decades) and very high temporal resolution are available at continuously operating stations, but logistics prevent installation of dense networks. InSAR, on the other hand, offers spatial resolution on the order of 10 s of meters with generally years-long time series, depending on the observing platform, but at temporal resolutions that vary between days to weeks, and surface displacements are resolved only in the one-dimensional line-of sight of the satellite. Steep terrain and long seasons of snow and ice cover also limit the applicability of InSAR for some regions. InSAR time series analysis is becoming routine in volcano monitoring (e.g., Grapenthin, Cheng, et al., 2022), but hinges on the longevity of SAR missions, the open availability of the SAR data, and rapid repeat times on the order of 6–12 days as the Sentinel-1 mission (Geudtner et al., 2014) and the future NISAR mission provide (Xaypraseuth et al., 2015). Lastly, tiltmeters are very sensitive to small deformation and offer high temporal resolution. While this makes them very sensitive to environmental noise driven by, for example, temperature or soil moisture change, they can capture signals well below the detection thresholds of InSAR or GNSS. The preference of one technique over another, or their combination, depends on factors like logistics, funding, and constraints imposed by the host rock and subsurface process behavior (Battaglia et al., 2019), and (in the case of SAR satellite data) often data availability and mission priorities.

Multiple codes have been released over the last decade to invert geodetic observations to resolve source properties. Battaglia et al. (2013a) provide MATLAB-based code (dModels) that accepts InSAR, GNSS, tilt and strainmeter data. They implemented four analytical models to estimate surface deformation in volcano-tectonic applications: spherical (McTigue, 1987), prolate spheroidal (X. M. Yang et al., 1988), penny-shaped crack (Fialko et al., 2001), rectangular dislocations (Okada, 1985) and superposition of rectangular dislocations (e.g., Jónsson et al., 2002). The dModels inversion technique is a weighted least squares algorithm and the package provides an *F*-test to detect overfitting of models to data. Bagnardi and Hooper (2017) also provide MATLAB-based code, the Geodetic Bayesian Inversion Software (GBIS), for InSAR and GNSS data analysis using the geodetic models from dModels and a Bayesian inversion approach using the Markov-Chain Monte Carlo (Markov Chain Monte-Carlo (MCMC)) method via the Metropolis-Hastings algorithm (Hastings, 1970). Trasatti (2022) implemented a Python-based code, the Volcanic and seismic source Modeling (VSM) that works with InSAR, GNSS, tilt, leveling and electronic distance measurement (EDM) data. This also supports inversions using multiple types of geodetic data and implements a global optimization algorithm and a Bayesian approach using the MCMC method.

Here, we introduce the VMOD inversion framework, fully written in Python. VMOD includes the most commonly used elastic analytic deformation models: isotropic point source (Mogi, 1958), spherical cavity (McTigue, 1987), rectangular dislocation source (Okada, 1985), prolate spheroidal cavity (X. M. Yang et al., 1988) and penny-shaped crack (Fialko et al., 2001). One of its main features, setting it apart from other

codes, is that it implements an object oriented paradigm (e.g., Booch, 1990) where the code is organized in classes, used to instantiate objects that interact in the program. This approach has several advantages over the functional programming that is more common for such applications, including a more natural representation of the problem in discrete classes, ease of expansion, and minimization of code redundancies. The problem of volcano deformation modeling separates into three main components: source model, data, and inversion. An object oriented implementation allows us to generalize these three components into base classes that provide common functionality (or interfaces) expected from any source model, data source, or inverse method enabling a straightforward combination of specific realizations of these components (e.g., Grapenthin, 2014). For instance, all data sources must contain coordinates at which the observations have been made, source models must provide a way to calculate displacements at these locations, and an inverse method needs to be able to combine models and data and evaluate some kind of misfit as a function of model parameters. Not only does such an architecture allow straightforward addition of new models, data sources, and inverse methods without having to modify the main components of the code, it also allows us to reuse existing models to implement more complex geometries. For instance, we include an implementation for discretized planar dislocations to explore slip distributions within a fault or heterogeneous opening of sills or dikes. Similarly, we include a circular discretized dislocation to represent ring fault as a model for volcanic calderas such as Sierra Negra in Galapagos, Ecuador (Bell et al., 2021). However, these simple kinematic models do not include time dependent processes, heterogeneity of the crust, or topography. Furthermore, for sources that are too deep the models cannot give accurate information about dimensions or overpressures (Segall, 2019). Therefore, besides the steady state models implemented in similar frameworks, VMOD distinguishes itself by also implementing models involving time-dependent crustal rheology such as a spherical source embedded in a viscoelastic half-space (Bonafede & Ferrari, 2009), a spherical source within a viscoelastic shell surrounded by an elastic half-space (Segall, 2010), an analytical solution for a pressurized well in a porelastic half-space (Wangen et al., 2018), and models involving time-dependent magma properties such as a pressurized open conduit that accounts for the physical properties of the magma (Nishimura, 2009).

VMOD's data component can handle different geodetic data types such as: GNSS, InSAR, tilt, level, and EDM. The framework can run joint inversions drawing from multiple data sets of different data types. It provides first order corrections for topography when observation location elevation values are provided. To reduce computational cost when InSAR data are used, VMOD also offers auxiliary functions to read data from downsampled CSV files or it can downsample interferograms itself (Jónsson et al., 2002). The inverse component provides a non-linear least squares solution or a Bayesian approach to obtain posterior distributions for the model parameters.

VMOD has been successfully applied to analyze deformation at several volcanoes (e.g., Cheng & Grapenthin, 2024; Grapenthin, Cheng, et al., 2022; Grapenthin, Kyle, et al., 2022) and to analyze deformation around a reinjection well (Graves et al., 2023). In this paper, we introduce its architecture and use, demonstrate its abilities in a series of verification and validation exercises, and use VMOD to infer a new magmatic source model for Westdahl volcano (an informal name for the volcano under Westdahl and Faris Peaks, Alaska) and Fisher Caldera on Unimak Island, Alaska, by jointly inverting continuous and campaign GNSS and InSAR data to constrain a multi-source model.

2. Method

Formally, we can relate observed data $\mathbf{d}$ with predictions of a source model $\mathbf{G}$ parameterized by a vector of model parameters $\mathbf{m}$ using

$$\mathbf{d} = \mathbf{G}(\mathbf{m}) + \sigma \tag{1}$$

where σ denotes data uncertainty. To implement a framework that enables the forward and inverse modeling captured in Equation 1, we employ an object oriented architecture. This minimizes code redundancy, creates flexibility to, for instance, allow users to choose between inversion strategies, and importantly, enables straightforward user-driven expansions to add new source models ($\mathbf{G}$), data types ($\mathbf{d}$), or inversion strategies. Thus, the main classes VMOD implements are *Inversion*, *Source* and *Data*. In the inverse approach, *Inversion* uses *Source* and *Data*, where the *Source* provides an abstract interface to any volcanic source model, handling the
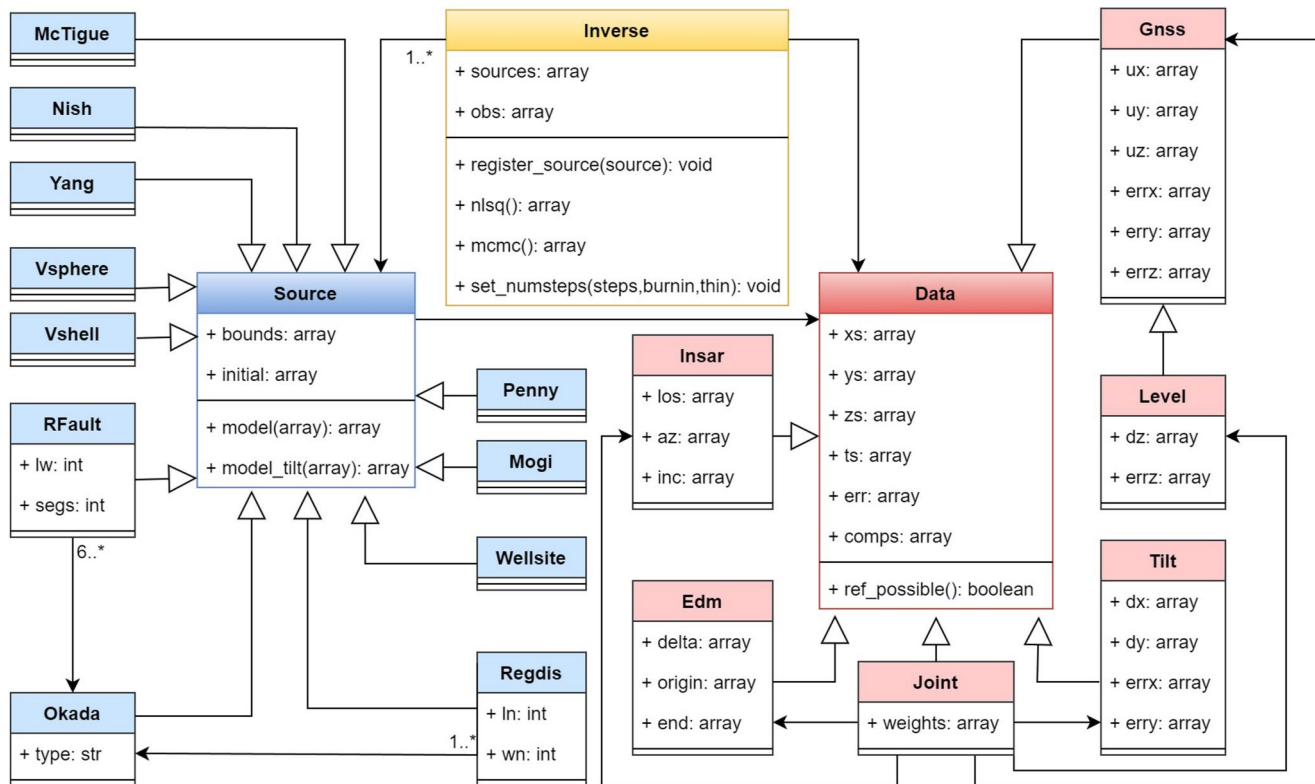
Figure 1. Class diagram describing the structure of the Versatile Modeling of Deformation. Each box represents a class, the upper segment has the name of the class, the middle segment shows the main attributes of the class and the lower segment contains the main methods in that class. For simplicity, we omitted details in some of the classes. Black headed arrows represent associations between classes (class at arrow origin uses class at arrow head). The associations are 1 to 1 unless the symbol X. * is next to the arrow which indicates that the association can be X to many. The white headed arrows indicate inheritance between classes (class at arrow origin inherits from class at arrow head). Colors associate functions: blue—source models; red—data types; yellow—inversion class.

common functions for forward models such as parameter bounds and initial values. The class *Data* abstracts from specific data types to allow for unified reading and handling of the input data. We explain each class below. The current capabilities of VMOD are captured in Figure 1.

2.1. Data Types

The "abstract" class *Data* implements the commonalities between the geodetic data types. These commonalities include the location points (attributes *xs*, *ys*), and optional attributes for elevation values (*zs*) and temporal values (*ts*). Similarly, we define the attribute *comps* to store the components that belong to a certain data type. For instance, the *comps* attribute for the *Gnss* class (GNSS datatype) includes the east, north and vertical displacement components. In the case of the *Insar* (InSAR datatype) the attribute *comps* only has the line-of-sight (LOS) displacement component. The structure for each of the datatypes is also the same (Figure 2b). If a new datatype is to be included, the user needs to define the components for that datatype. For example, the class *Insar* has the method *add_los* that adds the LOS components to the *comps* attribute. The user should also specify how to derive the component from the displacements in east, north and vertical with the method *from_model_3d*. For instance, LOS displacements can be computed from three-component (east, north, and vertical) displacements using the satellite azimuth and incidence angles (Figure 2a). We include five types of data: GNSS (*Gnss* class), InSAR (*Insar* class), tilt (*Tilt* class), EDM (*Edm* class), and leveling (*Level* class). VMOD allows *Data* objects that contain multiple data sets using the *Joint* class. The user can add data objects into a *Joint* object with the function *add_data set*, this function receives a data object and a relative weight between the different data sets that are added to the object. Although these weights are arbitrary and a user decision, we suggest taking into account the number of datapoints on each data set, so the data set with fewer datapoints has a larger relative weight. The framework also includes an auxiliary function to downsample InSAR data (Figure S1 in Supporting Information S1) using a quadtree technique driven by the data variance (Jónsson et al., 2002). This function reduces the

```
(a) class Insar(Data):
        def __init__(self):
            ...

        def add_los(self,los):
            self.add_comp(los,'los')
            self.los=los

        def from_model3d(self,func):
            ux,uy,uz=func(self.xs,self.ys)

            los=ux*np.sin(self.inc)*np.cos(self.az)-\
                uy*np.sin(self.inc)*np.sin(self.az)-\
                uz*np.cos(self.inc)

            los_ref=self.reference_dataset(los)

            return (-los_ref,)
```

```
(b) class Mogi(Source):
        def set_parnames(self):
            self.parameters=("xcen","ycen","depth","dV")
        def model(self,params):
            ...
            return ux, uy, uz
        def model_tilt(self,params):
            ...
            return dx, dy
        def model_t(self,params):
            ...
            return ux, uy, uz
```

Figure 2. Code examples. (a) *Insar* class code. The method *add_los* defines the only component belonging to the Interferometric Synthetic Aperture Radar (InSAR) datatype (Line of sight-LOS). The method *from_model3d* projects the 3D motion into the LOS using the azimuth angles (*self.az*) and incidence angles (*self.inc*). (b) *Mogi* class code. The method *set_parameters* defines the names and order for the parameters in the model. The method *model* returns the displacement in east, north and vertical for a steady-state model. The method *model_t* returns the displacement in east, north and vertical for a time dependent model. The method *model_tilt* returns the tilts using analytical expressions.

computational time required for inversions that use InSAR data. However, the user can use any algorithm to downsample an InSAR data set and provide this to VMOD. For instance, Lohman and Simons (2005) considered the covariance structure in the noise of InSAR data. VMOD expects a CSV file, which stores the downsampled observations.

2.2. Source Models

The "abstract" class *Source* is inherited and implemented by multiple sub-classes (Table S1 in Supporting Information S1). The *Mogi* class implements an isotropic point source model (Mogi, 1958), the *Mctigue* class implements a spherical pressurized cavity (McTigue, 1987), the *Okada* class implements the rectangular dislocation described in Okada (1985), the *Yang* class implements a prolate spheroidal cavity (X. M. Yang et al., 1988), the *Penny* class implements a penny-shaped crack model (Fialko et al., 2001), and the *Wellsite* class implements an analytical solution for a pressurized well in a porelastic medium (Wangen et al., 2018).

VMOD includes composite model implementations for a ring fault model (*RFault*) and a regularized sill/fault (*Regdis*), composed of multiple sill/fault patches. Both use the *Okada* class and provide different geometrical configurations of multiple rectangular dislocations or tensile patches, demonstrating the expansion potential of VMOD. In the ring fault model the patches are arranged to form an elliptic cylinder. The user decides the number of patches in the ring with the attributes *lw* (along depth) and *segs* (along length), by default *lw* = 1 and *segs* = 6. These patches are vertical faults to represent caldera collapse or uplift accommodated by a ring fault. This model solves for location, depth, semimajor and semiminor axes, strike, width of the patches, opening and slip. The opening/slip is uniform through all the patches and the user is expected to provide as an attribute the number of patches for the ring fault. The regularized sill/fault is comprised of tensile or slip patches arranged in a rectangular shape (Figure S2 in Supporting Information S1). The number of patches is a user decision and the opening/slip is controlled by a second order Tikhonov regularization (e.g., Aster et al., 2018). This model only solves for the opening/slip on each patch and the user has to provide the remaining parameters as attributes (location, depth, length, width, strike, dip, rake and the number of patches along length *ln* and along width *wn*). Users also provide a value for the regularization hyper-parameter that determines the model smoothness.

We also include models that consider magma reservoir rheology. Bonafede and Ferrari (2009) considered an isotropic pressurized point source in a viscoelastic medium, which is parameterized by a relaxation time and implemented by *Vsphere*. Segall (2010) model for a pressurized sphere inside a viscoelastic shell surrounded by an elastic medium, which we implement in *Vshell*. This model includes an additional parameter to describe the ratio between the outer and inner radius for the viscoelastic shell.

In the class *Nish* we implement an open conduit model that accounts for magma viscosity and represents subsurface processes for open system volcanoes (Nishimura, 2009). This class implements a steady state model and three time dependent models that account for three different magma rheology scenarios: (a) magma with low gas content such that bubbles do not grow inside the magma column, (b) when magma experiences bubble growth due to diffusive processes, and (c) when magma experiences bubble growth due to the migration and expansion of the bubbles inside the magma column.

The source model implementations calculate the deformation for the east, north and vertical components expected for the respective model, which can also be expressed relative to the calculated displacements at a reference station. The *Mogi*, *Mctigue*, *Okada*, and *Nish* classes include analytical expressions for tilt calculations. When analytical expressions for tilt are not available, the framework computes finite differences of the vertical displacements to derive ground tilt using the derivative function from the SciPy library (Virtanen et al., 2020) with a spacing of 1 μm. We also compute LOS displacements with range decrease as positive and viceversa. Similarly, when elevation values are defined in the *Data* class, we use the Williams and Wadge (1998) topography approximation which varies the depth of the source for each station or pixel according to its elevation value. However, this has been only validated for vertical displacements using the Mogi (1958) and McTigue (1987) models. This is also not advisable for near field solutions (Crozier et al., 2023).

The framework expects each model class to implement the same interface (Figure 2b). If users want to incorporate a new source model into VMOD, they have to create a new class with at least the methods *set_parameters* to define the parameters and *model* to implement a steady state model that outputs the deformation in east, north and vertical given a set of parameters. The user has the option to include a time dependent model by defining the method *model_t* (mandatory if the *Data* object contains time dependent observations). The *model* method uses the spatial coordinates (attributes *xs*, *ys*, *zs* in the *Data* object); the *model_t* method uses the spatial coordinates and the temporal coordinates (attribute *ts* in the *Data* object). Similarly, the user can define the displacement in three dimensions for different depths (with the method *model_depth*), if this method is defined the framework can calculate stresses.

2.3. Inversion

In an inverse problem we solve Equation 1 to determine the model parameters, $\mathbf{m}$, from the noisy observations, $\mathbf{d}$. Ideally, we want the model-predicted observables, $\mathbf{G(m)}$, to be within data uncertainties if these can be determined. Thus, a "best-fitting" solution can be estimated by minimizing a residual function $\mathbf{F(m)}$ (for simplicity given in a least squares sense here), which can be expressed as the norm of the difference between model predictions and the observations:

$$\begin{aligned} \mathbf{F(m)} &= \|\mathbf{G(m)} - \mathbf{d}\|_{L2}^2 \\ &= (\mathbf{G(m)} - \mathbf{d})^T \mathbf{C}_D^{-1} (\mathbf{G(m)} - \mathbf{d}) \end{aligned} \tag{2}$$

where $\mathbf{C}_D$ is the covariance matrix for the observations. We can minimize this function by calculating the gradient of the residual function ($\mathbf{\Gamma}(m)$) and solving for $\mathbf{m}$ where the gradient is zero ($\mathbf{\Gamma}(m) = 0$). For linear models, we can rewrite Equation 1 as $\mathbf{d} = \mathbf{Gm}$. Substituting this into Equation 2 and calculating the gradient we obtain a best-fitting solution with $\mathbf{m} = \left(\mathbf{G}^T \mathbf{C}_D^{-1} \mathbf{G}\right)^{-1} \mathbf{G}^T \mathbf{C}_D^{-1} \mathbf{d}$.

When the model is non-linear, we can approximate the residual function with the lower order terms of a Taylor series expansion using an initial set of parameters $\mathbf{m}_0$ that is close to our solution (i.e., $\mathbf{F(m)} = 0$). We can achieve a good approximation if we consider the second order terms in the Taylor expansion. Therefore, we need to calculate the gradient (first derivative) of the residual function and the Hessian (second derivative) of the residual function ($\mathbf{H(m_0)}$). Using this approximation we find that $\mathbf{m} = \mathbf{m}_0 - [\mathbf{H(m_0)}]^{-1} \mathbf{\Gamma(m_0)}$ (Tarantola, 2005).

One of the algorithms in this framework (*nlsq*) uses a gradient descent technique following the trust region reflective algorithm (Branch et al., 1999). This algorithm, implemented in the SciPy Python package (Virtanen et al., 2020), iteratively solves trust-region subproblems determined by the distance from the bounds and the direction of the gradient.

Alternatively, we may frame the inverse problem in a Bayesian sense and seek to determine the range of model parameters consistent with both data **d** and any independent (prior) information $\rho_M(\mathbf{m})$. In this approach the solution to the inverse problem is a posterior probability distribution $\sigma_M(\mathbf{m}|\mathbf{d})$ over all model parameters. Following Bayes' theorem:

$$\sigma_M(\mathbf{m}|\mathbf{d}) = k\rho_M(\mathbf{m})L(\mathbf{d}|\mathbf{m}) \tag{3}$$

where $L(\mathbf{d}|\mathbf{m})$ is the likelihood function which relates the model predictions and data, and k is a normalization constant. The likelihood distribution is often assumed a Gaussian distribution where $L(\mathbf{d}|\mathbf{m}) = e^{-\frac{1}{2}\mathbf{F(m,d)}}$.

For the Bayesian approach we sample the posterior distributions using a MCMC technique implemented in the PyMC package (Patil et al., 2010). MCMC samples from a posterior probability distribution that cannot be directly computed. Several approaches exist to implement MCMC sampling. The most popular is the Metropolis-Hastings algorithm (Hastings, 1970), which uses a random walker that at a given step $\mathbf{m}_i$ proposes a transition to a new point $\mathbf{m}_j$ using the prior distribution $\rho_M(\mathbf{m})$. Then, if $L(\mathbf{d}|\mathbf{m}_j) \geq L(\mathbf{d}|\mathbf{m}_i)$, the transition is accepted if not the probability that the transition is accepted is $L(\mathbf{d}|\mathbf{m}_j)/L(\mathbf{d}|\mathbf{m}_i)$.

In theory this algorithm generates samples proportional to the posterior distribution over the model parameters. However, the number of steps required to adequately characterize the distribution depends on the initial model parameters chosen, the number of parameters, and the complexity of the distribution. In some cases the algorithm may get caught in a local probability maximum. Therefore, the step sizes can be "tuned" to efficiently recover the posterior distribution. The "tuning" is a key factor when MCMC is applied; however, it can have a high computational cost, depending on the model that is being used. Hence, VMOD applies the Adaptive Metropolis-AM algorithm (Haario et al., 2001) which is a variation of the Metropolis-Hastings algorithm. The AM algorithm updates the step sizes along with the process using all values of likelihood accumulated so far. This algorithm reduces computation time because it avoids the typical trial-and-error methodology, where the step size is tested using the results of short chains (Rosenthal, 2011). The PyMC includes a wide catalog of samplers, such as the traditional Metropolis-Hastings (Hastings, 1970), the Slice sampler (Neal, 2003), or the Gibbs sampler (Geman & Geman, 1984). The user can replace the inversion algorithm or add a new one with little effort.

All parameters in every model are treated as stochastic variables with uniform prior distributions. Initial guesses for parameter values are also required. After the inversion is completed, VMOD offers the option to display the histograms for each parameter using the library *corner* from Foreman-Mackey et al. (2016). VMOD's MCMC chains by default are composed of 1 million steps; however, this depends on how many parameters the model has. To reduce autocorrelation, we retain only the solution for every 1000th step (thinning), which will be larger as the number of estimated model parameters increases. We also delete a model-dependent number of steps at the beginning of the chain (burn-in) to eliminate any bias introduced by the choice of the initial parameter values (Aster et al., 2018). These are default numbers used by VMOD; however, the user can change these modifying the method *set_numsteps* in the *Inverse* class.

Figure S3a–S3f in Supporting Information S1 offers a minimal recipe on how to run an inversion. The user must specify *Data*, *Model*, and *Inversion* objects. The user can also define a joint data set, in case more than one data set is available. The *Inverse* object also expects a *Data* object as a parameter. The user can include more than one deformation source to run an inversion (Figure S3f in Supporting Information S1).

3. Benchmarking

3.1. Source Models

To validate our implementations of the analytical models we test them against well-proven published implementations and reproduce characteristic figures from the literature (Figures S4 and S5 in Supporting Information S1). We also participated in the Drivers of Volcano Deformation (DVD) community exercise (Crozier et al., 2023), the purpose of which was to verify and validate geodetic model implementations (Figure S6 in Supporting Information S1).

We first compare VMOD against the MATLAB-based dModels code (Battaglia et al., 2013a), which has been benchmarked with numerical finite element model (FEM) simulations. The results are summarized in Figure S4a–

S4d in Supporting Information S1. We find excellent reproduction of dModels predictions by VMOD for our implementations of the point source (Mogi, 1958) and pressurized sphere (McTigue, 1987) (Figure S4a in Supporting Information S1), the prolate spheroid (X. M. Yang et al., 1988) (Figure S4b in Supporting Information S1), the tensile dislocation (Okada, 1985) (Figure S4c in Supporting Information S1), and the penny-shaped crack (Fialko et al., 2001) models (Figure S4d in Supporting Information S1).

For the Nishimura (2009) steady state solution, we reproduce the vertical displacement of Figure 4 in Nishimura (2009) in our Figure S4e in Supporting Information S1. Here, we find an offset in the two results that is due to a difference in the scale factor for the normalization according to the author (T. Nishimura, written communication, 20 January 2021), corroborating the correct implementation in VMOD. We replicate figures in the Nishimura (2009) manuscript for the three cases (Figure S5a in Supporting Information S1).

For Bonafede and Ferrari (2009) and Segall (2010) models, we reproduce figures from the original manuscripts (Figure S5b in Supporting Information S1). However, in the reproduction of the Bonafede and Ferrari (2009) figure, the original paper's results are scaled by a factor of 4, meaning that the computations actually used either a pressure of 400 MPa or shear modulus of 1 GPa, as opposed to the reported values. This has been confirmed with the author (M. Bonafede, written communication, 24 June 2023). In Figure S5b in Supporting Information S1 we used a shear modulus of 1 GPa.

To further test VMOD, we participated in the DVD (Crozier et al., 2023) community geodetic model verification exercise. DVD specifies four forward model scenarios of pressurized sources, and we participate with VMOD in three of these, providing the requested solutions for displacement and stress fields. The first exercise required modeling a pressurized sphere embedded in an elastic half-space. For this, we use our McTigue (1987) implementation, which gives solutions within rounding error of the DVD dModels solution (Battaglia et al., 2013a), as expected per our test above, and is similar to the FEM solutions. The second exercise consists of a pressurized sphere embedded in an elastic half-space with simple volcanic edifice topography. We apply our semi-analytical approximation from Williams and Wadge (1998) and the McTigue (1987) model. Our results agree with the FEM solutions in the far field. However, in the near field, within a radial distance of about 1 source depth, the vertical deformation is underestimated up to 30% and the horizontal deformation is overestimated by 40% (Figure S6 in Supporting Information S1), showing that in the near field the flat half-space assumption of the analytical model does not hold for topography. The third exercise requires modeling an oblate spheroid embedded in an elastic half-space. VMOD does currently not include a model implementation for this problem. However, the ratio between the semimajor and semiminor axes for the spheroid is low (ratio = 0.1). Therefore, we use the Fialko et al. (2001) solution for a penny-shaped crack. Our results are similar to the FEM solutions. Although we cannot use this result as a verification for our model, we can say that the implementation of the Fialko et al. (2001) solution in VMOD is valid for an oblate spheroid with a low ratio of its semiaxes (Figure S7 in Supporting Information S1).

3.2. Inversion Algorithm

We test the inversion algorithms first by creating noisy synthetic data from which we try to recover the known parameters. The synthetic data are the product of the deformation produced by a forward model using the X. M. Yang et al. (1988) implementation and the values shown by the red stars in Figure S8 in Supporting Information S1 plus white noise with a maximum amplitude of 20% of the deformation value. The true values used to create the synthetic data always fall inside or close to the 95% confidence level when we use the Bayesian inversion and the non-linear least squares solution. However, the accuracy of the retrieved values depends on the noise level and the possible tradeoff between the parameters. For instance, for the X. M. Yang et al. (1988) model we have a tradeoff between the dimensions of the spheroid and the pressure (Figures S8 and S9 in Supporting Information S1).

We furthermore tested the inversions through a DVD validation exercise for the blind estimation of model parameters from noisy, synthetic observations. All that was known about these observations was that they are due to pressurization of a spherical source in an elastic half space (Zhong et al., 2019). Participants were provided with six synthetic data sets: four InSAR data sets (high and low noise for ascending and descending observations) and two GNSS data sets (high and low noise) (Table S2 in Supporting Information S1). The participants could choose to either jointly or separately invert the GNSS and InSAR data sets for the high and low signal-to-noise ratio (SNR) cases.
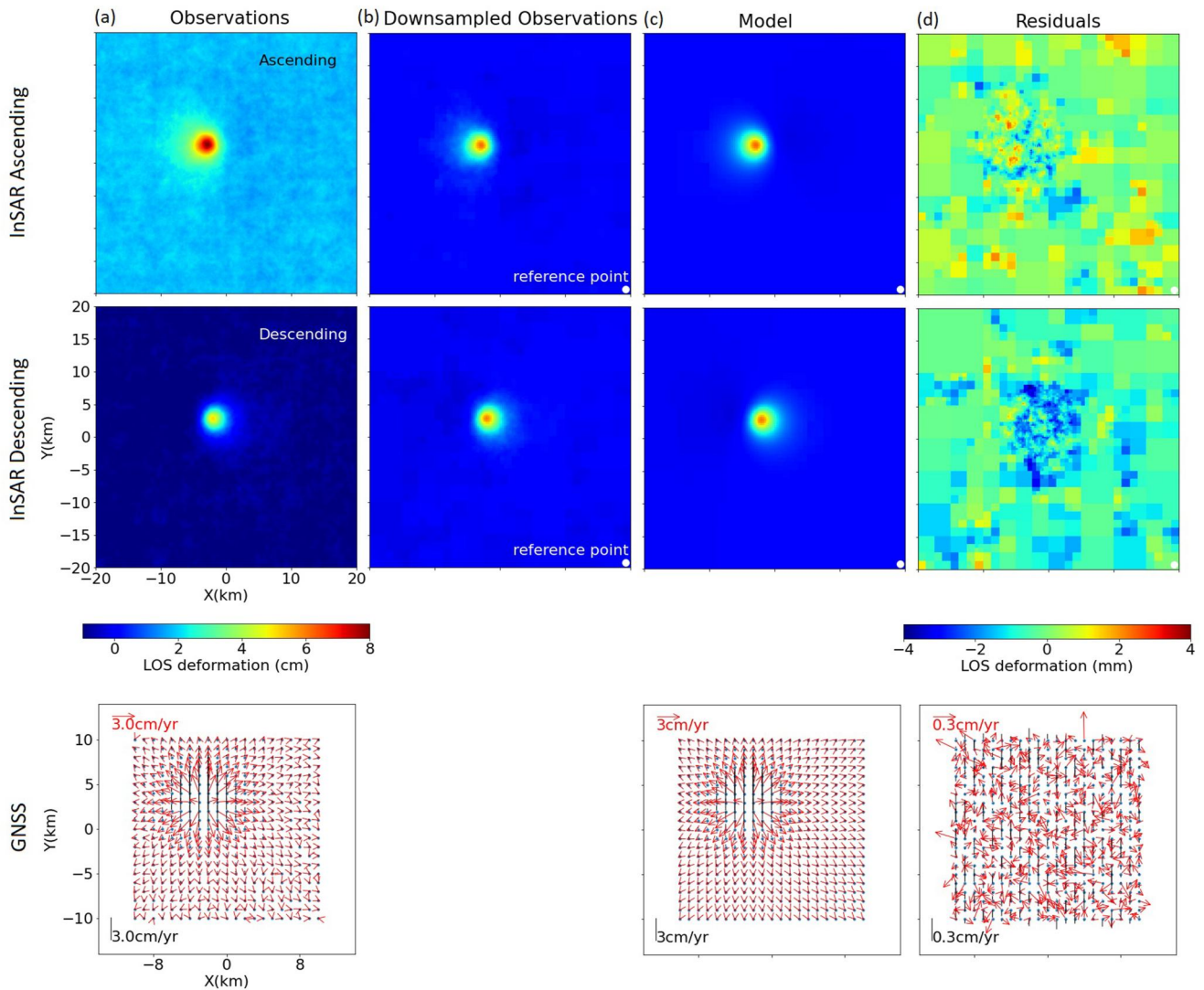
Figure 3. Joint solution for the Drivers of Volcano Deformation inversion exercise for the low signal-to-noise ratio (SNR) data sets. (a) Synthetic data sets with low SNR, first row shows the Interferometric Synthetic Aperture Radar (InSAR) observations in the ascending track, second row shows the InSAR deformation in the descending track, third row shows the Global Navigation Satellite System (GNSS) observations. (b) Downsampled measurements for the InSAR data sets. The white points represent the reference pixel in the images. (c) Deformation fields using the model from maximum a posteriori in the posterior distributions from the joint Bayesian inversion. (d) Model residuals in the GNSS and InSAR data sets.

While VMOD includes implementations for the Mogi (1958) model and the McTigue (1987) model, which both could be used for this exercise, the Mogi (1958) model is poorly suited for shallow sources. Therefore, we use the McTigue (1987) model and solve for five parameters (x-location, y-location, depth, radius, and pressure) when using the GNSS data. Then we calculate the volume change with the empirical formula in Battaglia et al. (2013b). When we use the InSAR data sets, we also solved for the offsets (biases) in the ascending and descending tracks. We obtained solutions for both high and low SNR inversion exercises that follow the same strategy (Figures S10–S16 in Supporting Information S1). In total we performed three inversions for each SNR case: one using the ascending and descending InSAR data sets (Figures S10–S11 and S14–S15 in Supporting Information S1), one using the GNSS data set (Figures S10, S12, S14, and S16 in Supporting Information S1), and a third inversion that uses all data jointly (Figure 3, Figures S10, S13, and S14 in Supporting Information S1). For the latter we do not solve for the offsets. Instead, we take a reference pixel to eliminate background noise and align the InSAR and GNSS data (Figure 3). Although the measurements within the data sets are automatically weighted depending on their uncertainties, the relative weight between data sets is up to the user. However, in this case we choose the same weight because we have a considerable amount of GNSS observations
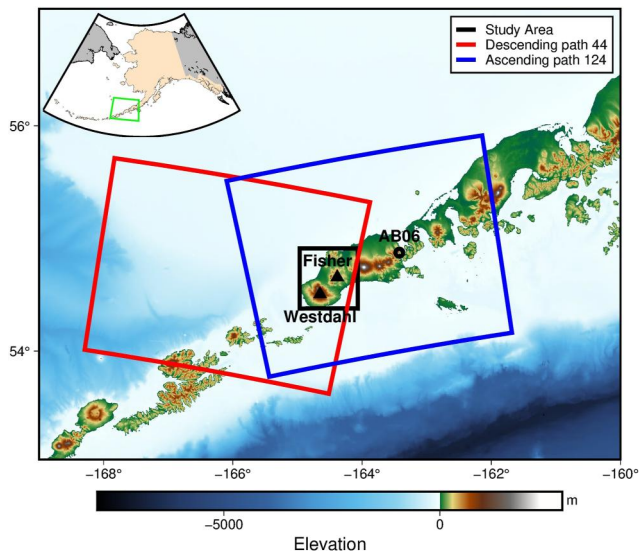
Figure 4. Unimak Island location. Red and blue squares represent the sizes of the Sentinel-1 ascending and descending Synthetic Aperture Radar scenes. The black box shows the study area that includes Westdahl volcano and Fisher Caldera (black triangles). The black circle shows the location of the reference station AB06.

available (442 stations $*$ 3 components $=$ 1,320 observations) compared with the downsampled InSAR observations (2,000 pixels per track).

Our results overlap with or are close to the mean results of other participants in the DVD exercises (Table S2, Figures S10 and S14 in Supporting Information S1). The confidence intervals are also comparable. However, the posterior distributions using just the GNSS data sets are wider than the ones using just the InSAR data sets or all data sets at the same time (e.g., Figures S10 and S14 in Supporting Information S1). This is a consequence of including more information in our inversion that can better constrain the model parameters.

In most cases the non-linear least squares solution and the Bayesian maximum a posteriori (MAP) solution coincide. However, in some cases the least squares solution is caught in a local minimum. Although these solutions are close to the solutions from other participants, with the least squares solution alone it is not possible to explore the tradeoff between the parameters or the uncertainty in the results (e.g., radius vs. pressure in Figure S14 in Supporting Information S1).

4. Case Study: Westdahl Volcano and Fisher Caldera

Inversions that systematically test superpositions of multiple deformation sources that jointly analyze (and test contributions of) different data sources are rarely seen in deformation studies. Usually the deformation signals are isolated and studied individually (Gong et al., 2015). Similarly, the deformation observations from different techniques are analyzed separately (Mann & Freymueller, 2003). However, especially with the proliferation of InSAR through open data, surface deformation is now often detected by more than one geodetic technique (for instrumented volcanoes), or in both ascending and descending directions of SAR satellites. This can reveal otherwise unrecognized complexity of the deformation field (Grapenthin, Cheng, et al., 2022), requiring straightforward modeling of multiple deformation sources that might act at the same time.

Westdahl volcano and Fisher Caldera, located on Unimak Island at the western tip of the Alaska Peninsula (Figure 4), is a complex use case as the volcanic centers are close to each other (10–15 km) and have been nearly continuously deforming over the last 30 years. This deformation has been observed with InSAR (Gong et al., 2015; Lu et al., 2000, 2003) and campaign and continuous GNSS observations (Freymueller, 1998, 2000, 2002a, 2002b; Grapenthin & Angarita, 2021; Mann & Freymueller, 2003). In this case the deformation signals at Westdahl volcano and Fisher Caldera cannot be separated from each other just by limiting the spatial scale of the deformation field (Figure 4). Thus, we use VMOD to jointly invert the GNSS and InSAR data sets for the parameters of two deformation sources.

Located in the arc overlying part of the Alaska-Aleutian subduction zone with a plate interface with a low degree of coupling (e.g., Drooff & Freymueller, 2021; Mann & Freymueller, 2003; Xiao et al., 2021), Westdahl volcano last erupted in 1991–1992 (Miller et al., 1998), while Fisher Caldera, with a caldera forming eruption 9,400 years ago, last erupted with a small explosive eruption in 1826 (Stelling et al., 2005). Given their history, several studies have previously analyzed Westdahl volcano and Fisher Caldera using different geodetic data (InSAR, GNSS) and various modeling approaches. Lu et al. (2000) infer an inflating point source 8.7 km deep, with a volume change of 0.05 km^3 using ERS-1/2 interferograms from 1993 to 1998. This point source was also inferred by Mann and Freymueller (2003) who used GNSS campaign observations from 1998 to 2001. They resolved a point source under Westdahl volcano at a depth of ~7 km that was inflating at a rate of 6.7 Mm^3/yr and suggest a contracting dike ~2 km deep as a source for Fisher Caldera deformation deflating at a rate of ~2.3 Mm^3/yr. Lu et al. (2003) modeled the evolution for the change of volume in the magma reservoir as an exponential decay trend. They proposed that the magma flow rate through the conduit is governed by a pressure gradient between a deep source and a shallower reservoir and argued that when the magma supply is exhausted the eruption stops and the reservoir begins to pressurize again. Gong et al. (2015) performed an inversion for a point source (Mogi, 1958) under Westdahl volcano using the results from a persistent scattering interferometry from the ENVIronmental SATellite advanced synthetic aperture radar (ENVISAT) where they discarded the pixels outside the volcanic
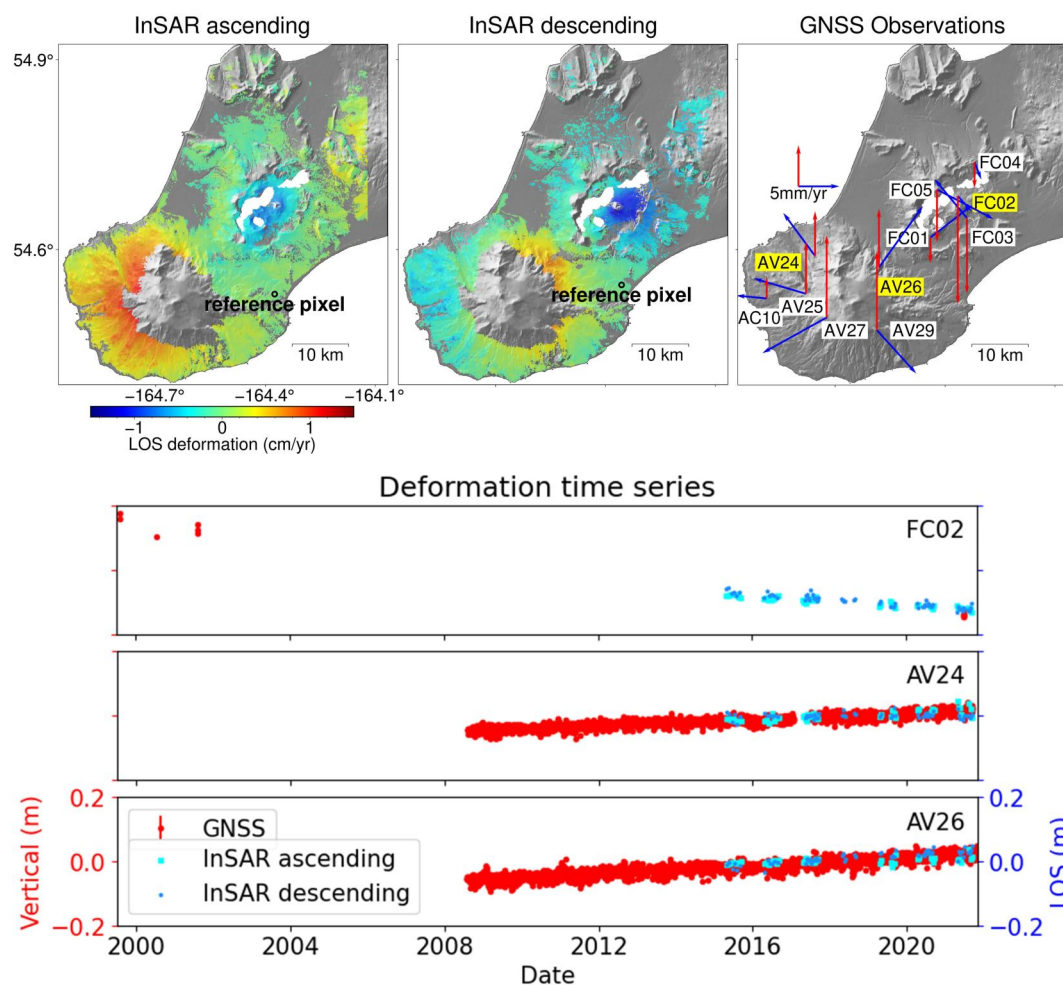
Figure 5. Interferometric Synthetic Aperture Radar (InSAR) and Global Navigation Satellite System (GNSS) observations. (a) Velocity rate map for the InSAR (from 2015 to 2021) and GNSS observations (from 2001 to 2021 for Fisher Caldera and from 2008 to 2021 for Westdahl volcano). (b) Time series for the vertical velocities for the stations FC02, AV24, and AV26 with respect to AB06 and time series for the line-of-sight deformation in the closest pixel to each station in the ascending and descending directions.

edifice. Similarly, they inverted for the parameters of an Okada (1985) model at Fisher Caldera, discarding pixels at Westdahl volcano. Their results suggested an inflating point source with a rate of 2.7 Mm^3/yr, ~7 km deep under Westdahl volcano and a contracting sill with a rate 1.4 Mm^3/yr, ~5 km deep at Fisher Caldera. Also, they speculated the long-term decaying process is a consequence of episodic injections of magma. For Fisher Caldera, they suggested a contraction of magma as a consequence of crystallization and degassing or depressurization of the hydrothermal system. Xue and Freymueller (2020) analyzed the GNSS measurements after the 1992 eruption until 2019 and used previous InSAR results from Lu et al. (2003) and Gong et al. (2015) to support the hypothesis that the arrival of discrete pulses of new magma explains the stair-stepping behavior in time of the magma pressure.

In addition to 6 continuous GNSS stations at Westdahl volcano going back to the summer of 2008, and prior campaigns at Westdahl volcano and Fisher Caldera (Freymueller, 1998, 2000, 2002a, 2002b), new GNSS campaign observations were collected in June 2021 at all Fisher Caldera benchmarks (Grapenthin & Angarita, 2021). The data processing strategy follows that of Grapenthin, Kyle, et al. (2022). The resulting timeseries (Figure S17 in Supporting Information S1) confirm the subsidence observed in previous studies. We complemented these observations with summer to summer interferometric pairs from the Sentinel 1 A/B mission spanning 2016 to 2021 (Figure 5). We obtain the interferometric pairs (Figure S18 in Supporting Information S1) from the Alaska Satellite Facility's vertex portal (Kennedy et al., 2021) and use interferograms with high
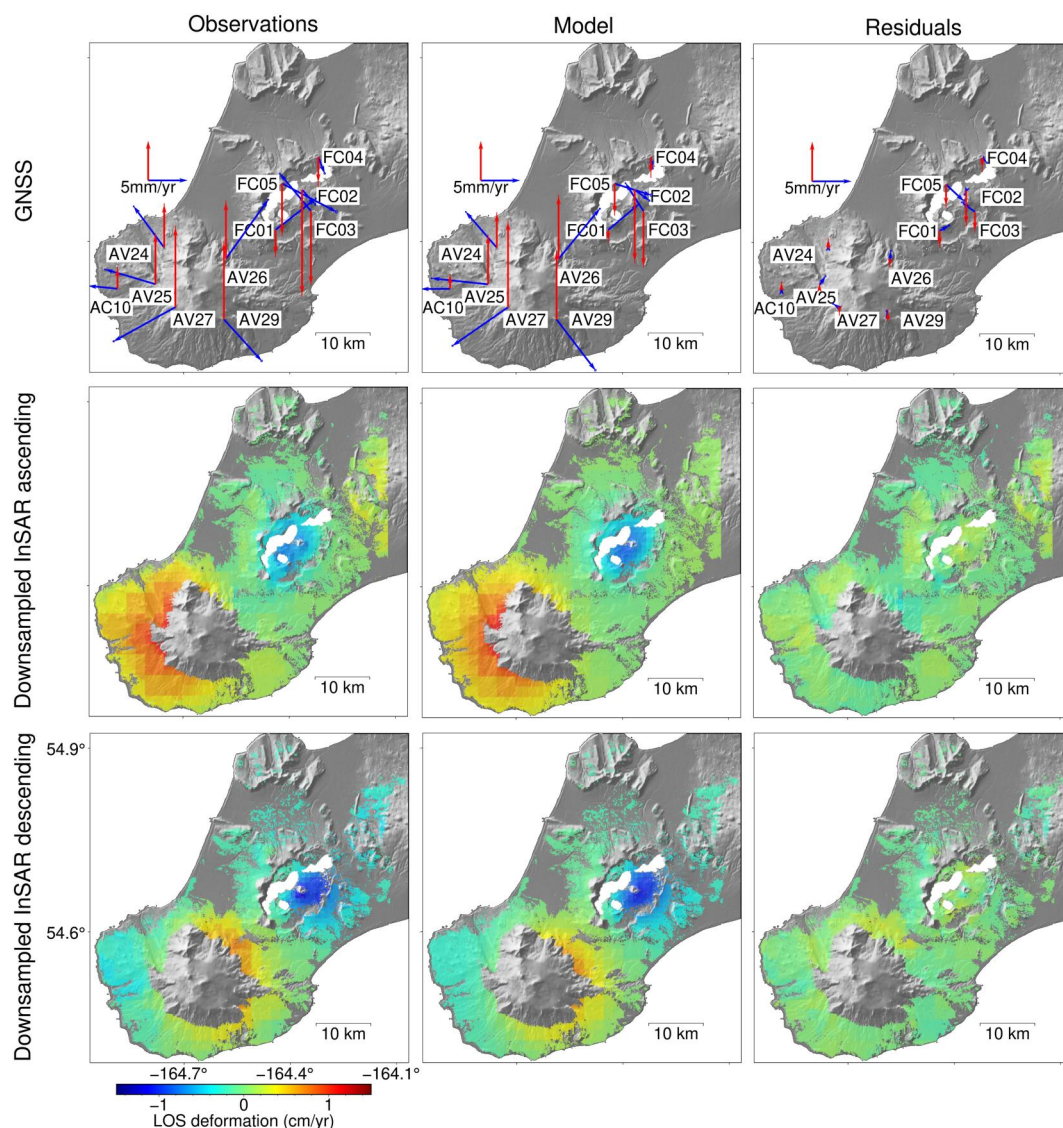
Figure 6. Deformation observations and results for the inversion at Westdahl volcano and Fisher Caldera using all data sets jointly. First column, observed data sets, first row shows the Global Navigation Satellite System (GNSS) observations, second row shows the downsampled Interferometric Synthetic Aperture Radar (InSAR) observations in the ascending track, third row shows the downsampled InSAR deformation in the descending track. The black point represents the reference pixel. Second column, deformation fields using the maximum a posteriori value from the joint Bayesian inversion. Third column, model residuals for the GNSS and downsampled InSAR data sets.

coherence values (>0.7) to generate InSAR time series with MintPy (Yunjun et al., 2019) as detailed in Grapenthin, Cheng, et al. (2022). We downsample the resulting cumulative displacements using the quadtree method described above to reduce the computational cost. We kept 800 points for the ascending direction and 895 points for the descending direction. The InSAR results agree with the GNSS observations with an uplift rate at Westdahl volcano of ~ 1.5 cm/yr in the LOS direction (Figure 6).

We use VMOD to infer the possible sources that could explain the observed deformation. We try several models with two pressure sources (two spherical sources, spherical source and sill/dike source and spherical source and spheroidal source). We perform multiple inversions (Figures 6 and 7, Figures S19–S24 in Supporting Information S1) using the GNSS observations (Figure 7, Figures S19 and S21 in Supporting Information S1), using the ascending and descending InSAR observations jointly (Figure 7, Figures S20, S21, and S23 in Supporting Information S1), and using all GNSS and InSAR data simultaneously (Figures 6 and 7, Figures S21 and S24 in
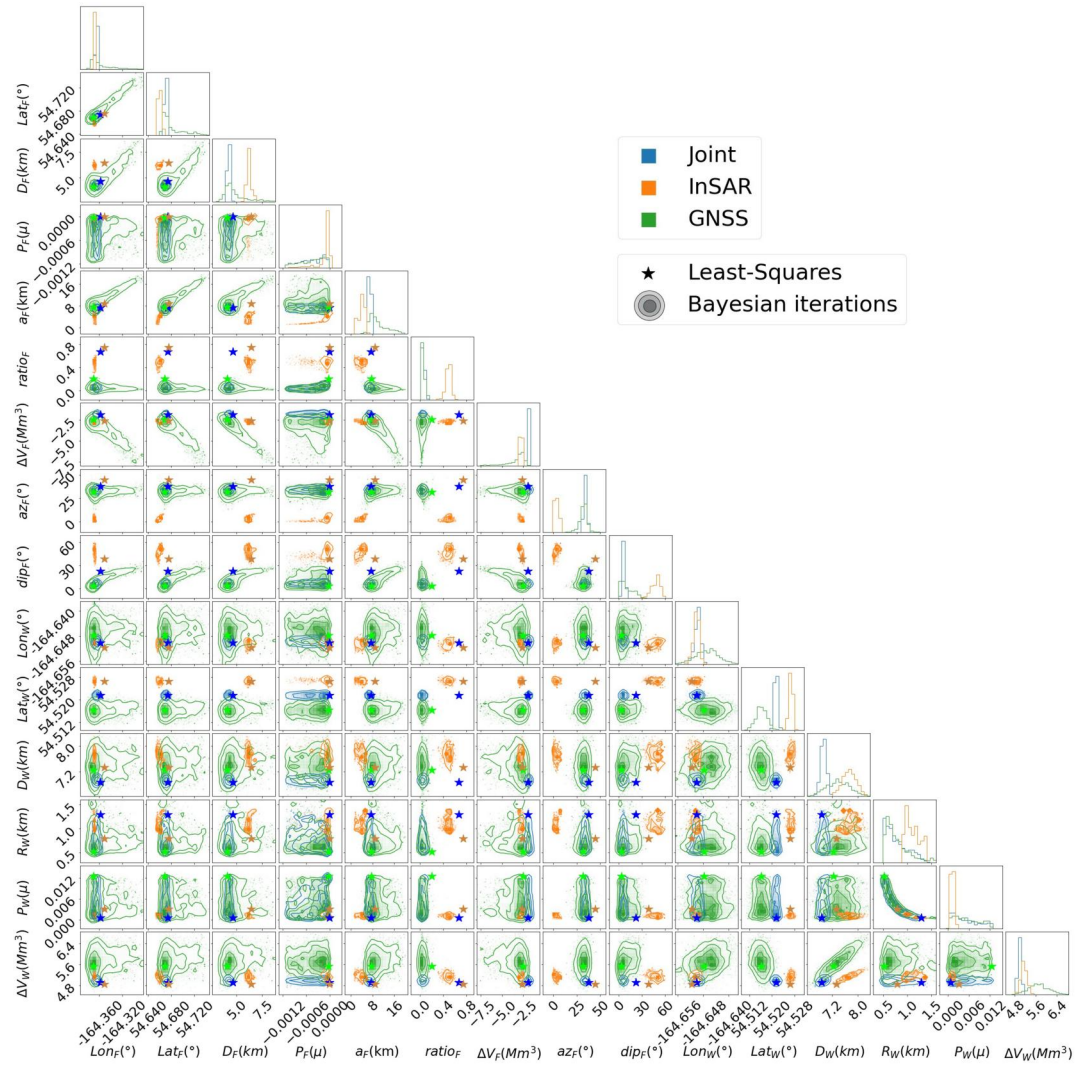
Figure 7. Histograms showing the posterior distributions for each of the parameters in the prolate spheroidal and spherical model for Fisher Caldera and Westdahl volcano. The colors represent the data set used for the inversion: blue for the joint data set, orange for the Interferometric Synthetic Aperture Radar (InSAR) and green for the Global Navigation Satellite System. The stars represent the results from the least squares inversions. *Lon* and *Lat* represent the longitude and latitude, *D* is the depth, ΔV is the volume change, *a* is the semimajor axis, ratio is the semiminor axis divided by the semimajor axis, *az* is the azimuth angle, *dip* is the dipping angle. The subindex *F* refers to the spheroidal source for Fisher Caldera, the subindex *W* refers to the spherical source for Westdahl volcano.

Supporting Information S1). We assigned a bigger relative weight to the GNSS data set as it has fewer observations than the InSAR data set. We achieve the best fit (Table 1) using a spherical source (McTigue, 1987) under Westdahl volcano and a prolate spheroid (X. M. Yang et al., 1988) under Fisher Caldera. Some parameter values differ between the inversions depending on the data set (InSAR, GNSS or joint) (Table 2). However, the inversions suggest a spherical source at 7–8 km depth, and a spheroidal source at 4.5–6.5 km depth. The change in volume for the spherical model indicates an average magma supply of 5 Mm^3/yr at Westdahl volcano and a volume loss at Fisher Caldera at rate of ∼2–3 Mm^3/yr. These volume changes are calculated using the empirical expression from Battaglia et al. (2013b). We calculate the traces for the volume changes a posteriori using the traces from pressure dimensions and depth (Figure 7).

Table 1

Root Mean Square Error (RMSE) for the Best Fitting Models for Fisher Caldera and Westdahl Volcano

Model	Data set	GNSS (cm/year)	InSAR (cm/year)
Spherical and sill/dike	GNSS	0.09	–
	InSAR	–	0.11
	Joint	0.15	0.12
Spherical and spheroidal	GNSS	0.06	–
	InSAR	–	0.10
	Joint	0.14	0.11

Note. The "Model" column specifies the sources used in the model. The "Data set" column describes the data set used in the inversion. "Global Navigation Satellite System (GNSS)" is the RMSE in the GNSS data set and the "Interferometry of Synthetic Aperture Radar (InSAR)" column is the RMSE in the InSAR data set.

5. Discussion

One of the main features of VMOD is the easy integration of new models or new data types. The models have evolved in complexity from a pressurized point source (Mogi, 1958), to spheroidal or spherical shapes (McTigue, 1987; X. M. Yang et al., 1988) or new geometric shapes like sill, penny-shaped cracks or dikes (Fialko et al., 2001; Okada, 1985). Currently, models can include viscoelastic processes (Bonafede & Ferrari, 2009) or magma rheology (Nishimura, 2009). Also, geodetic data types have evolved in coverage and accuracy from leveling measurements in the nineteenth century to the use of tiltmeters at volcanoes in the early twentieth century, GNSS observations in the late 1980s and InSAR observations in the early 1990s. Although there are several inversion codes such as dModels (Battaglia et al., 2013a) or GBIS (Bagnardi & Hooper, 2017), incorporation of a new data type or a new model into a package can be difficult or even impossible in cases when we do not have access to a proprietary software license. And while some frameworks may be written in open source, high-level programming languages and facilitate customization (e.g., Trasatti, 2022), VMOD provides well-specified interfaces (*Source, Data, Inverse*, Figure 1) that allow the addition of new models (e.g., Bonafede & Ferrari, 2009; Nishimura, 2009; Segall, 2010), straightforward combination of existing models for forward (e.g., regularized sill/faults and ring fault models) and inverse applications, or data sources by simply providing a new class that inherits from the respective base class, without having to alter the core VMOD code. The framework also allows inversion using multiple data types at the same time with multiple inversion algorithms. Crozier et al. (2023) showed a surprising dependency of model results on the chosen inversion methodology, which makes straightforward change or addition of inversion strategies an important feature of frameworks like VSM (Trasatti, 2022) and VMOD.

The validation exercises from the DVD community show that analytical solutions implemented by VMOD like the McTigue (1987) and Fialko et al. (2001) are a good alternative when FEM models are not available and the source depth is much larger than its dimensions. While the deformation is underestimated in the near field, the differences in the mid and far field (>1 km) are negligible (Figure S6a in Supporting Information S1).

Table 2

Inversion Results for Westdahl Volcano and Fisher Caldera With Columns for Results and 95% Confidence Intervals Using Global Navigation Satellite System (GNSS) Data, Interferometry of Synthetic Aperture Radar (InSAR) Data, and a Joint Inversion of all Data

Source	Parameter	GNSS	InSAR	Joint
Fisher	Longitude (°)	$-164.364^{+0.062}_{-0.011}$	$-164.368^{+0.002}_{-0.003}$	$-164.364^{+0.002}_{-0.002}$
	Latitude (°)	$54.674^{+0.009}_{-0.054}$	$54.660^{+0.006}_{-0.004}$	$54.670^{+0.001}_{-0.001}$
	Depth (km BMSL)	$4.51^{+3.24}_{-0.80}$	$6.19^{+0.45}_{-0.34}$	$4.25^{+0.17}_{-0.17}$
	Pressure (μ/yr)	$-0.00041^{+0.00033}_{-0.00062}$	$-0.00004^{+0.00002}_{-0.00050}$	$-0.00050^{+0.00040}_{-0.00060}$
	Volume change (Mm³/yr)	$-3.00^{+0.79}_{-3.73}$	$-2.76^{+0.24}_{-0.27}$	$-1.85^{+0.09}_{-0.09}$
	Semimajor axis (km)	$9.01^{+8.00}_{-2.82}$	$4.13^{+1.69}_{-2.55}$	$6.92^{+0.47}_{-0.47}$
	Semiminor axis (km)	$0.39^{+0.52}_{-0.16}$	$2.00^{+1.13}_{-1.21}$	$0.33^{+0.39}_{-0.11}$
	Azimuth (°)	32^{+5}_{-8}	3^{+5}_{-3}	34^{+3}_{-3}
	Dipping (°)	8^{+17}_{-7}	50^{+6}_{-12}	7^{+3}_{-3}
Westdahl	Longitude (°)	$-164.647^{+0.006}_{-0.007}$	$-164.650^{+0.001}_{-0.002}$	$-164.650^{+0.002}_{-0.002}$
	Latitude (°)	$54.516^{+0.003}_{-0.003}$	$54.527^{+0.001}_{-0.001}$	$54.521^{+0.001}_{-0.001}$
	Depth (km BMSL)	$7.38^{+0.65}_{-0.62}$	$7.75^{+0.30}_{-0.37}$	$6.93^{+0.14}_{-0.15}$
	Pressure (μ/yr)	$0.0049^{+0.0065}_{-0.0041}$	$0.0012^{+0.0078}_{-0.0006}$	$0.0043^{+0.0074}_{-0.0034}$
	Volume change (Mm³/yr)	$5.70^{+0.75}_{-0.64}$	$5.14^{+0.19}_{-0.19}$	$4.98^{+0.11}_{-0.10}$
	Radius (km)	$0.71^{+0.65}_{-0.17}$	$1.10^{+0.29}_{-0.17}$	$0.72^{+0.52}_{-0.21}$

Note. The parameters for the Fisher Caldera source describe a prolate spheroidal source (X. M. Yang et al., 1988). The parameters for Westdahl volcano source describe a spherical source (McTigue, 1987). The pressures are given in terms of the shear modulus (μ).

Furthermore, exercise 2 shows how the Williams and Wadge (1998) approximation is valid for the vertical displacements in the far field (>2 km) (Figure S6b in Supporting Information S1). These exercises showcase some of the capabilities of the framework and the different options to invert for volcanic sources. One of these options is being able to choose to invert for offsets in the InSAR data sets. In the joint inversion, we can see a small bias to negative values for the low and high SNR that we do not see in the inversion using just the InSAR data set. The results from this exercise suggest that solving for the offsets is more appropriate when using InSAR data sets. However, if the number of data sets is substantial, we would have an excessive number of parameters. Besides, the InSAR data sets can show non-constant offsets. Therefore, in some cases—such as when InSAR data show orbital ramp errors—we suggest to correct the InSAR data sets before inverting for deformation sources. Our posterior distributions and those of the other participants are close in almost all parameters. However, we find some discrepancies in depth, radius and pressure indicating tradeoffs between those parameters for the spherical model. The results reveal the non-uniqueness for the McTigue (1987) implementation for the spherical model. This tradeoff has been observed for other analytical models (Albright & Gregg, 2020) like the dimensions of a dislocation and the opening for a sill or a dike (Okada, 1985) or the dimensions and the pressure in a spheroidal model (X. M. Yang et al., 1988). Additionally, analytical models cannot consider heterogeneities in the crust or topography. Some of these limitations from the analytical models can be overcome by new implementations from FEM models or Boundary Element Methods (Cayol & Cornet, 1997), along with the development of new geodetic datatypes.

Our case study for Westdahl volcano and Fisher Caldera highlights two main features of VMOD: (a) the ease of testing multi-source models and (b) the ease of jointly inverting GNSS and InSAR observations. In previous attempts at these volcanoes, the deformation signals have been isolated for each system or each geodetic technique has been analyzed independently. However, the deformation field from Westdahl volcano's magma reservoir can influence the observed deformation at Fisher Caldera and vice versa given their close proximity, and GNSS and InSAR data sets each have advantages and disadvantages. Therefore, we jointly invert all the available observations. Mann and Freymueller (2003) suggested a dike geometry as the most probable source but their bootstrap analysis showed that a sill (dipping angle between 0 and 20°) could also explain the deformation pattern. Moreover, Gong et al. (2015) inferred a sill-like source to explain the deformation in Fisher Caldera. In our analysis, we try different geometric sources, including the sill/dike geometry source suggested by Mann and Freymueller (2003) and Gong et al. (2015). Although a sill/dike source can explain the InSAR data, and GNSS individually (Figures S21–S23 in Supporting Information S1), the azimuth angle changes drastically depending on the data set (Figure S21 in Supporting Information S1). On the other hand, the joint inversion shows systematic misfit in the stations FC02, FC03, and FC05 for the GNSS data set (Figures S21 and S24 in Supporting Information S1). We find that a prolate spheroid can explain the deformation in the three data sets (Figure 7). We also observe agreement in almost all the parameters for both sources including locations, depths, length of semimajor axis, pressures and volume changes. Nevertheless, we have some differences in the ratio between the semimajor and semiminor axes and the dipping angle for the spheroidal source. These discrepancies can be attributed to the remaining uncertainties in the campaign sites and atmospheric noises that remains after the SBAS processing, and also the different time intervals covered by the data sets—in essence we assume a constant process, while we know that the deformation rates are time varying (Figure 2a, Xue & Freymueller, 2020).

Our results at Westdahl volcano and Fisher Caldera coincide with previous results from Gong et al. (2015) and Mann and Freymueller (2003), including depths and volume changes (Table S3 in Supporting Information S1). However, the dislocation inferred by Mann and Freymueller (2003) is shallower (∼2 km) than our spheroid (∼4–6 km). However, their inversion showed a bimodal distribution allowing a horizontal and deeper sill (4–5 km) as a possible solution (Figure 4a in Mann and Freymueller (2003)). In most cases, the non-linear least squares inversion results (Figure 7) have a higher Root Mean Square Error than the Bayesian inversions, this might be a consequence of local minimums in the parameter space that gradient based algorithm cannot escape. Whereas the Bayesian inversions discarded these minimums in the burn-in period. Something of significance to point out are the biases data set choices can introduce into the modeling. Our inversions using the InSAR data sets result in different solutions depending on the viewing geometry. We observe significant disagreements in some parameters if we use only the descending or ascending direction (Figure S25 in Supporting Information S1). For instance, the locations for both sources and the volume change in the spherical source are not similar. Similar biases have been observed by Grapenthin, Cheng, et al. (2022) at Mount Edgecumbe where a dipping sill could explain the deformation pattern observed in the descending geometry for a preliminary analysis but it was not able to explain

the deformation patterns observed in two ascending images. In their final analysis, the most probable model indicates a transcrustal migration of magma between a contracting dipping sill at 20 km and a inflating point source at 10 km. Although our multi-source models do not account for source interactions (Pascal et al., 2014), VMOD enables straightforward testing of such multi-source models tests and joint inversions, especially in monitoring situations where the data availability can change rapidly over time.

The purpose of VMOD is to integrate new models from the scientific community so we can test broad model suites and more useful geodetic models. We are constantly expanding the code. For instance, the compound dislocation model has been implemented in VMOD (Nikkhoo et al., 2017), but still requires some additional validation and verification (Figure S26 in Supporting Information S1). Future iterations of this framework could include for example, a systematic way to evaluate possible source(s) that replicate the observed deformation. So far this process has been executed manually. The main issue is the computational cost to run multiple Bayesian inversions at the same time and the number of steps necessary to achieve convergence. Finite element representations such as geodetic models using convolutional neural networks (DeVries et al., 2017) or Gaussian stochastic process emulators (e.g., Anderson et al., 2019; Gu & Berger, 2016) could be used in VMOD. Furthermore, new inversion algorithms such as the Ensemble Kalman Filter (e.g., Zhan & Gregg, 2017) could be easily included using the object-oriented structure that we implement for VMOD.

6. Conclusions

We have developed an object-oriented Python-based deformation inversion framework called VMOD suitable for InSAR, GNSS, tilt, leveling, and EDM data. The framework includes the most common elastic models such as the point source (Mogi, 1958), the spherical cavity (McTigue, 1987), the spheroidal cavity (X. M. Yang et al., 1988), penny-shaped crack (Fialko et al., 2001), and rectangular dislocation (Okada, 1985). We also include some time-dependent models such as the open conduit model (Nishimura, 2009) and an implementation for injection wells (Wangen et al., 2018). VMOD's architecture allows for easy integration of new geodetic data types and new geodetic models. It also allows for the extension and reuse of existing models to create new source geometries. For instance, include implementations for ring fault models and regularized sills/faults composed of smaller rectangular dislocation models. We benchmarked our forward and inverse modeling framework by replicating published results and as a part of a community volcano deformation model verification exercise (Battaglia et al., 2013a; Crozier et al., 2023; Segall, 2010). We use the framework to simultaneously characterize two deformation sources at Unimak Island for Westdahl volcano and Fisher Caldera using InSAR data, and continuous and campaign GNSS data, including observations from a new campaign at Fisher Caldera. Although a sill/dike geometry has been suggested in the past for Fisher Caldera; it cannot explain the InSAR and GNSS data sets simultaneously. Our results suggest a depressurizing spheroid for Fisher Caldera $\sim$4–6 km deep, contracting at a rate of $\sim$2–3 Mm^3/yr, and a pressurized spherical source for Westdahl volcano $\sim$7–8 km deep, inflating at a rate of $\sim$5 Mm^3/yr. The VMOD framework has been used for other volcanic unrest (Grapenthin, Cheng, et al., 2022) demonstrating the advantages of jointly inverting multiple data sets using multiple source models. In the future, we envision VMOD expansions with more geodetic models and new inversion algorithms that can capture the physics of subsurface processes.

Data Availability Statement

The Sentinel 1 SAR data analyzed from paths 44 (frame 410) and 124 (frame 176) during summer acquisitions (May to August) from 2015 to 2021 are available through ESA (https://dataspace.copernicus.eu/) and ASF DAAC (https://search.asf.alaska.edu/). The Zenodo repository (https://doi.org/10.5281/zenodo.10070627) contains the codes and notebooks implementing the methods developed here (Angarita et al., 2023). The repository is continuously updated in Github (https://github.com/uafgeotools/vmod/).

References

Albright, J. A., & Gregg, P. M. (2020). Distinguishing inflation drivers at shallow magmatic systems using Ensemble-based data assimilation. In *IGARSS 2020-2020 IEEE international geoscience and remote sensing symposium* (pp. 3622–3625).

Anderson, K. R., Johanson, I. A., Patrick, M. R., Gu, M., Segall, P., Poland, M. P., et al. (2019). Magma reservoir failure and the onset of caldera collapse at Kīlauea Volcano in 2018. *Science*, *366*(6470), eaaz1822. https://doi.org/10.1126/science.aaz1822

Angarita, M., Grapenthin, R., Henderson, S., Christoffersen, M., & Anderson, K. (2023). Versatile modeling of deformation (VMOD) inversion framework [Software]. *Zenodo*. https://doi.org/10.5281/zenodo.10070627

Angarita, M., Grapenthin, R., Plank, S., Meyer, F. J., & Dietterich, H. (2022). Quantifying large-scale surface change using SAR amplitude images: Crater morphology changes during the 2019–2020 Shishaldin volcano eruption. *Journal of Geophysical Research: Solid Earth*, *127*(8), e2022JB024344. https://doi.org/10.1029/2022jb024344

Aster, R. C., Borchers, B., & Thurber, C. H. (2018). *Parameter estimation and inverse problems*. Elsevier.

Bagnardi, M., & Hooper, A. J. (2017). GBIS (Geodetic Bayesian Inversion Software): Rapid inversion of InSAR and GNSS data to estimate surface deformation source parameters and uncertainties. In *AGU fall meeting abstracts* (Vol. 2017, p. G23A-0881).

Battaglia, M., Alpala, J., Alpala, R., Angarita, M., Arcos, D., Euillades, L., et al. (2019). Monitoring volcanic deformation. In *Reference module in Earth systems and environmental sciences*. Elsevier B.

Battaglia, M., Cervelli, P. F., & Murray, J. R. (2013a). dMODELS: A MATLAB software package for modeling crustal deformation near active faults and volcanic centers. *Journal of Volcanology and Geothermal Research*, *254*, 1–4. https://doi.org/10.1016/j.jvolgeores.2012.12.018

Battaglia, M., Cervelli, P. F., & Murray, J. R. (2013b). *Modeling crustal deformation near active faults and volcanic centers: A catalog of deformation models and modeling approaches (technical report)*. US Geological Survey. https://doi.org/10.3133/tm13B1

Bell, A. F., La Femina, P. C., Ruiz, M., Amelung, F., Bagnardi, M., Bean, C. J., et al. (2021). Caldera resurgence during the 2018 eruption of Sierra Negra volcano, Galápagos Islands. *Nature Communications*, *12*(1), 1397. https://doi.org/10.1038/s41467-021-21596-4

Biggs, J., & Pritchard, M. E. (2017). Global volcano monitoring: What does it mean when volcanoes deform? *Elements*, *13*(1), 17–22. https://doi.org/10.2113/gselements.13.1.17

Bonafede, M., & Ferrari, C. (2009). Analytical models of deformation and residual gravity changes due to a Mogi source in a viscoelastic medium. *Tectonophysics*, *471*(1–2), 4–13. https://doi.org/10.1016/j.tecto.2008.10.006

Booch, G. (1990). *Object oriented design with applications*. Benjamin-Cummings Publishing Co., Inc.

Branch, M. A., Coleman, T. F., & Li, Y. (1999). A subspace, interior, and conjugate gradient method for large-scale bound-constrained minimization problems. *SIAM Journal on Scientific Computing*, *21*(1), 1–23. https://doi.org/10.1137/s1064827595289108

Cashman, K. V., & Sparks, R. S. J. (2013). How volcanoes work: A 25 year perspective. *GSA Bulletin*, *125*(5–6), 664–690. https://doi.org/10.1130/b30720.1

Cayol, V., & Cornet, F. (1997). 3D mixed boundary elements for elastostatic deformation field analysis. *International Journal of Rock Mechanics and Mining Sciences*, *34*(2), 275–287. https://doi.org/10.1016/s0148-9062(96)00035-6

Cheng, Y., & Grapenthin, R. (2024). The Alaska Makushin Volcano 2016–2018 inflation and its potential relation to the 2020 earthquake swarm, from GNSS observations. *Journal of Volcanology and Geothermal Research*, *446*, 108010. https://doi.org/10.1016/j.jvolgeores.2024.108010

Crozier, J., Karlstrom, L., Montgomery-Brown, E., Angarita, M., Cayol, V., Bato, M. G., et al. (2023). Understanding the drivers of volcano deformation through geodetic model verification and validation. *Bulletin of Volcanology*, *85*(12), 74. https://doi.org/10.1007/s00445-023-01687-4

DeVries, P. M., Thompson, T. B., & Meade, B. J. (2017). Enabling large-scale viscoelastic calculations via neural network acceleration. *Geophysical Research Letters*, *44*(6), 2662–2669. https://doi.org/10.1002/2017gl072716

Drooff, C., & Freymueller, J. T. (2021). New constraints on slip deficit on the Aleutian megathrust and inflation at Mt. Veniaminof, Alaska from repeat GPS measurements. *Geophysical Research Letters*, *48*(4), e2020GL091787. https://doi.org/10.1029/2020gl091787

Ebmeier, S., Biggs, J., Mather, T., Elliott, J., Wadge, G., & Amelung, F. (2012). Measuring large topographic change with InSAR: Lava thicknesses, extrusion rate and subsidence rate at Santiaguito volcano, Guatemala. *Earth and Planetary Science Letters*, *335*, 216–225. https://doi.org/10.1016/j.epsl.2012.04.027

Elliott, J., & Freymueller, J. T. (2020). A block model of present-day kinematics of Alaska and western Canada. *Journal of Geophysical Research: Solid Earth*, *125*(7), e2019JB018378. https://doi.org/10.1029/2019jb018378

Elliott, J. L., Grapenthin, R., Parameswaran, R. M., Xiao, Z., Freymueller, J. T., & Fusso, L. (2022). Cascading rupture of a megathrust. *Science Advances*, *8*(18), eabm4131. https://doi.org/10.1126/sciadv.abm4131

Fernández, J., Pepe, A., Poland, M. P., & Sigmundsson, F. (2017). Volcano Geodesy: Recent developments and future challenges. *Journal of Volcanology and Geothermal Research*, *344*, 1–12. https://doi.org/10.1016/j.jvolgeores.2017.08.006

Fialko, Y., Khazan, Y., & Simons, M. (2001). Deformation due to a pressurized horizontal circular crack in an elastic half-space, with applications to volcano geodesy. *Geophysical Journal International*, *146*(1), 181–190. https://doi.org/10.1046/j.1365-246x.2001.00452.x

Foreman-Mackey, D., Hogg, D. W., Lang, D., & Goodman, J. (2016). corner.py: Scatterplot matrices in Python. *Journal of Open Source Software*, *1*(2), 24. https://doi.org/10.21105/joss.00024

Fournier, N., & Chardot, L. (2012). Understanding volcano hydrothermal unrest from geodetic observations: Insights from numerical modeling and application to White Island volcano, New Zealand. *Journal of Geophysical Research*, *117*(B11), B11208. https://doi.org/10.1029/2012jb009469

Freymueller, J. (1998). Westdahl 1998 [Dataset]. *The GAGE Facility operated by EarthScope Consortium*. https://doi.org/10.7283/546R-QF59

Freymueller, J. (2000). Westdahl 1999 [Dataset]. *The GAGE Facility operated by EarthScope Consortium*. https://doi.org/10.7283/ZWNZ-MV02

Freymueller, J. (2002a). Westdahl 2000 [Dataset]. *The GAGE Facility operated by EarthScope Consortium*. https://doi.org/10.7283/581D-3F24

Freymueller, J. (2002b). Westdahl 2001 [Dataset]. *The GAGE Facility operated by EarthScope Consortium*. https://doi.org/10.7283/HKHZ-YK92

Geman, S., & Geman, D. (1984). Stochastic relaxation, Gibbs distributions, and the Bayesian restoration of images. *IEEE Transactions on Pattern Analysis and Machine Intelligence*, *6*, 721–741. https://doi.org/10.1109/tpami.1984.4767596

Geudtner, D., Torres, R., Snoeij, P., Davidson, M., & Rommen, B. (2014). Sentinel-1 system capabilities and applications. In *2014 IEEE geoscience and remote sensing symposium* (pp. 1457–1460).

Gong, W., Meyer, F., Lee, C.-W., Lu, Z., & Freymueller, J. (2015). Measurement and interpretation of subtle deformation signals at Unimak Island from 2003 to 2010 using weather model-assisted time series InSAR. *Journal of Geophysical Research: Solid Earth*, *120*(2), 1175–1194. https://doi.org/10.1002/2014jb011384

Grapenthin, R. (2014). CRUSDE: A plug-in based simulation framework for composable CRUstal DEformation studies using Green's functions. *Computers & Geosciences*, *62*, 168–177. https://doi.org/10.1016/j.cageo.2013.07.005

Grapenthin, R., & Angarita, M. (2021). Westdahl 2021 [Dataset]. *The GAGE Facility operated by EarthScope Consortium*. https://doi.org/10.7283/8QJD-EE25

Grapenthin, R., Cheng, Y., Angarita, M., Tan, D., Meyer, F. J., Fee, D., & Wech, A. (2022). Return from dormancy: Rapid inflation and seismic unrest driven by transcrustal magma transfer at Mt. Edgecumbe (L'úx Shaa) volcano, Alaska. *Geophysical Research Letters*, *49*(20), e2022GL099464. https://doi.org/10.1029/2022gl099464

Grapenthin, R., Kyle, P., Aster, R. C., Angarita, M., Wilson, T., & Chaput, J. (2022). Deformation at the open-vent Erebus volcano, Antarctica, from more than 20 years of GNSS observations. *Journal of Volcanology and Geothermal Research*, *432*, 107703. https://doi.org/10.1016/j.jvolgeores.2022.107703

Graves, E., Rinehart, A., Grapenthin, R., Angarita, M., & Grigg, J. (2023). InSAR-observed surface deformation in New Mexico's Permian Basin shows threats and opportunities presented by leaky injection wells. *Scientific Reports*, *13*(1), 17308. https://doi.org/10.1038/s41598-023-42696-9

Gu, M., & Berger, J. O. (2016). Parallel partial Gaussian process emulation for computer models with massive output.

Haario, H., Saksman, E., & Tamminen, J. (2001). An adaptive Metropolis algorithm. *Bernoulli*, *7*(2), 223–242. https://doi.org/10.2307/3318737

Hastings, W. K. (1970). Monte Carlo sampling methods using Markov chains and their applications. *Biometrika*, *57*(1), 97–109. https://doi.org/10.1093/biomet/57.1.97

Heap, M. J., Villeneuve, M., Albino, F., Farquharson, J. I., Brothelande, E., Amelung, F., et al. (2020). Towards more realistic values of elastic moduli for volcano modelling. *Journal of Volcanology and Geothermal Research*, *390*, 106684. https://doi.org/10.1016/j.jvolgeores.2019.106684

Jónsson, S., Zebker, H., Segall, P., & Amelung, F. (2002). Fault slip distribution of the 1999 Mw 7.1 Hector Mine, California, earthquake, estimated from satellite radar and GPS measurements. *Bulletin of the Seismological Society of America*, *92*(4), 1377–1389. https://doi.org/10.1785/0120000922

Kennedy, J., Anderson, R., Biessel, R., Chase, T., Ellis, O., Fairbanks, K., et al. (2021). Skip the processing: On demand analysis-ready InSAR from ASF. In *AGU fall meeting abstracts* (Vol. 2021, p. G45B-0395).

Lohman, R. B., & Simons, M. (2005). Some thoughts on the use of InSAR data to constrain models of surface deformation: Noise structure and data downsampling. *Geochemistry, Geophysics, Geosystems*, *6*(1), Q01007. https://doi.org/10.1029/2004gc000841

Lu, Z., Masterlark, T., Dzurisin, D., Rykhus, R., & Wicks, C. (2003). Magma supply dynamics at Westdahl volcano, Alaska, modeled from satellite radar interferometry. *Journal of Geophysical Research*, *108*(B7), 2354. https://doi.org/10.1029/2002jb002311

Lu, Z., Wicks, C., Dzurisin, D., Thatcher, W., Freymueller, J. T., McNutt, S. R., & Mann, D. (2000). Aseismic inflation of Westdahl volcano, Alaska, revealed by satellite radar interferometry. *Geophysical Research Letters*, *27*(11), 1567–1570. https://doi.org/10.1029/1999gl011283

Mann, D., & Freymueller, J. (2003). Volcanic and tectonic deformation on Unimak Island in the Aleutian Arc, Alaska. *Journal of Geophysical Research*, *108*(B2), 101. https://doi.org/10.1029/2002jb001925

Masterlark, T. (2003). Finite element model predictions of static deformation from dislocation sources in a subduction zone: Sensitivities to homogeneous, isotropic, Poisson-solid, and half-space assumptions. *Journal of Geophysical Research*, *108*(B11), 2540. https://doi.org/10.1029/2002jb002296

Masterlark, T. (2007). Magma intrusion and deformation predictions: Sensitivities to the Mogi assumptions. *Journal of Geophysical Research*, *112*(B6), W3CDTF. https://doi.org/10.1029/2006jb004860

McTigue, D. (1987). Elastic stress and deformation near a finite spherical magma body: Resolution of the point source paradox. *Journal of Geophysical Research*, *92*(B12), 12931–12940. https://doi.org/10.1029/jb092ib12p12931

Miller, T. P., McGimsey, R. G., Richter, D. H., Riehle, J. R., Nye, C. J., Yount, M. E., & Dumoulin, J. A. (1998). *Catalog of the historically active volcanoes of Alaska. United States Department of the Interior*. United States Geological Survey. https://doi.org/10.3133/ofr98582

Mogi, K. (1958). Relations between the eruptions of various volcanoes and the deformations of the ground surfaces around them. *Earthquake Research Institute*, *36*, 99–134.

Neal, R. M. (2003). Slice sampling. *Annals of Statistics*, *31*(3), 705–767. https://doi.org/10.1214/aos/1056562461

Nikkhoo, M., Walter, T. R., Lundgren, P. R., & Prats-Iraola, P. (2017). Compound dislocation models (CDMs) for volcano deformation analyses. *Geophysical Journal International*, *208*(2), 877–894. https://doi.org/10.1093/gji/ggw427

Nishimura, T. (2009). Ground deformation caused by magma ascent in an open conduit. *Journal of Volcanology and Geothermal Research*, *187*(3–4), 178–192. https://doi.org/10.1016/j.jvolgeores.2009.09.001

Okada, Y. (1985). Surface deformation due to shear and tensile faults in a half-space. *Bulletin of the Seismological Society of America*, *75*(4), 1135–1154. https://doi.org/10.1785/bssa0750041135

Pascal, K., Neuberg, J., & Rivalta, E. (2014). On precisely modelling surface deformation due to interacting magma chambers and dykes. *Geophysical Journal International*, *196*(1), 253–278. https://doi.org/10.1093/gji/ggt343

Patil, A., Huard, D., & Fonnesbeck, C. J. (2010). PyMC: Bayesian stochastic modelling in Python. *Journal of Statistical Software*, *35*(4), 1. https://doi.org/10.18637/jss.v035.i04

Poland, M., Hamburger, M., & Newman, A. (2006). The changing shapes of active volcanoes: History, evolution, and future challenges for volcano geodesy. *Journal of Volcanology and Geothermal Research*, *150*(1–3), 1–13. https://doi.org/10.1016/j.jvolgeores.2005.11.005

Rosenthal, J. S. (2011). Optimal proposal distributions and adaptive MCMC. In *Handbook of Markov Chain Monte Carlo, 4(10.1201)*.

Segall, P. (2010). *Earthquake and volcano deformation*. Princeton University Press.

Segall, P. (2019). Magma chambers: What we can, and cannot, learn from volcano geodesy. *Philosophical Transactions of the Royal Society A*, *377*(2139), 20180158. https://doi.org/10.1098/rsta.2018.0158

Sigmundsson, F., Hooper, A., Hreinsdóttir, S., Vogfjörd, K. S., Ófeigsson, B. G., Heimisson, E. R., et al. (2015). Segmented lateral dyke growth in a rifting event at Bárðarbunga volcanic system, Iceland. *Nature*, *517*(7533), 191–195. https://doi.org/10.1038/nature14111

Stelling, P., Gardner, J. E., & Begét, J. (2005). Eruptive history of Fisher caldera, Alaska, USA. *Journal of Volcanology and Geothermal Research*, *139*(3–4), 163–183. https://doi.org/10.1016/j.jvolgeores.2004.08.006

Tarantola, A. (2005). *Inverse problem theory and methods for model parameter estimation*. SIAM.

Trasatti, E. (2022). Volcanic and seismic source modeling: An open tool for geodetic data modeling. *Frontiers in Earth Science*, *10*, 917222. https://doi.org/10.3389/feart.2022.917222

Virtanen, P., Gommers, R., Oliphant, T. E., Haberland, M., Reddy, T., Cournapeau, D., et al. (2020). SciPy 1.0: Fundamental algorithms for scientific computing in Python. *Nature Methods*, *17*(3), 261–272. https://doi.org/10.1038/s41592-019-0686-2

Wangen, M., Halvorsen, G., Gasda, S. E., & Bjørnarå, T. (2018). An analytical plane-strain solution for surface uplift due to pressurized reservoirs. *Geomechanics for Energy and the Environment*, *13*, 25–34. https://doi.org/10.1016/j.gete.2018.03.002

Williams, C. A., & Wadge, G. (1998). The effects of topography on magma chamber deformation models: Application to Mt. Etna and radar interferometry. *Geophysical Research Letters*, *25*(10), 1549–1552. https://doi.org/10.1029/98gl01136

Xaypraseuth, P., Satish, R., & Chatterjee, A. (2015). NISAR spacecraft concept overview: Design challenges for a proposed flagship dual-frequency SAR mission. In *2015 IEEE Aerospace conference* (pp. 1–11).

Xiao, Z., Freymueller, J. T., Grapenthin, R., Elliott, J. L., Drooff, C., & Fusso, L. (2021). The deep Shumagin gap filled: Kinematic rupture model and slip budget analysis of the 2020 Mw 7.8 Simeonof earthquake constrained by GNSS, global seismic waveforms, and floating InSAR. *Earth and Planetary Science Letters*, *576*, 117241. https://doi.org/10.1016/j.epsl.2021.117241

Xue, X., & Freymueller, J. T. (2020). A 25-year history of volcano magma supply in the east central Aleutian arc, Alaska. *Geophysical Research Letters*, *47*(15), e2020GL088388. https://doi.org/10.1029/2020gl088388

Yang, Q., Zhao, W., Dixon, T. H., Amelung, F., Han, W. S., & Li, P. (2015). InSAR monitoring of ground deformation due to CO_2 injection at an enhanced oil recovery site, West Texas. *International Journal of Greenhouse Gas Control*, *41*, 20–28. https://doi.org/10.1016/j.ijggc.2015.06.016

Yang, X. M., Davis, P. M., & Dieterich, J. H. (1988). Deformation from inflation of a dipping finite prolate spheroid in an elastic half-space as a model for volcanic stressing. *Journal of Geophysical Research*, *93*(B5), 4249–4257. https://doi.org/10.1029/jb093ib05p04249

Yunjun, Z., Amelung, F., & Aoki, Y. (2021). Imaging the hydrothermal system of Kirishima volcanic complex with L-band InSAR time series. *Geophysical Research Letters*, *48*(11), e2021GL092879. https://doi.org/10.1029/2021gl092879

Yunjun, Z., Fattahi, H., & Amelung, F. (2019). Small baseline InSAR time series analysis: Unwrapping error correction and noise reduction. *Computers & Geosciences*, *133*, 104331. https://doi.org/10.1016/j.cageo.2019.104331

Zhan, Y., & Gregg, P. M. (2017). Data assimilation strategies for volcano geodesy. *Journal of Volcanology and Geothermal Research*, *344*, 13–25. https://doi.org/10.1016/j.jvolgeores.2017.02.015

Zhong, X., Dabrowski, M., & Jamtveit, B. (2019). Analytical solution for the stress field in elastic half-space with a spherical pressurized cavity or inclusion containing eigenstrain. *Geophysical Journal International*, *216*(2), 1100–1115. https://doi.org/10.1093/gji/ggy447